Multitask Graph Neural Networks for Elastoplastic Response Prediction in Dual-Phase Polycrystals*

Erdem Caliskan[1], Anik Das Anto[1], Massimiliano Lupo Pasini[2], Stephanie TerMaath[1], Reza Abedi[1*]

[1]Department of Mechanical and Aerospace Engineering, University of Tennessee Knoxville, 1506 Middle Drive, Knoxville, 37916, TN, USA.
[2]Computational Sciences and Engineering Division, Oak Ridge National Laboratory, 1 Bethel Valley Rd, Oak Ridge, 37831, TN, USA.

*Corresponding author(s). E-mail(s): rabedi@utk.edu;
Contributing authors: ecalisk1@vols.utk.edu; aanto@vols.utk.edu; lupopasinim@ornl.gov; stermaat@utk.edu;

Abstract

Microstructure-sensitive prediction of elastoplastic response remains a recurring bottleneck in multiscale damage and fatigue modeling, where large ensembles of statistically distinct polycrystals are required to quantify variability and extreme-value behavior. In this work, we develop a multitask graph neural network (GNN) surrogate that maps dual-phase ferrite–martensite polycrystal microstructures to Statistical Volume Element (SVE)-level elastoplastic quantities of interest. Each SVE is represented as a grain-adjacency graph, with node features encoding phase, geometry, and crystallographic orientation, and edge features encoding relative misorientation. A message-passing graph convolution generates node embeddings, which are pooled into a graph representation and passed to a multitask regression head that jointly predicts 10 scalar QoIs and vector-valued

stress–strain responses in orthogonal loading directions across multiple martensite volume fractions and SVE sizes. Results show high accuracy for scalar QoIs and strong agreement for full stress–strain trajectories, with population envelopes reproducing both median behavior and finite-SVE variability across compositions and partition scales. A unified model trained on pooled volume-fraction data preserves most within-regime accuracy relative to regime-specific models while also capturing the broader cross-regime variation reflected in the pooled test set. Distributional comparisons further demonstrate that the surrogate preserves heterogeneity under SVE partitioning, enabling statistically consistent blockwise random-field construction for mesoscale analyses. Overall, the proposed grain-graph surrogate provides a practical pathway to accelerate ensemble-based studies of constitutive variability relevant to crack nucleation and early-stage damage.

Keywords: Graph neural networks, Polycrystals, Crystal plasticity, Statistical volume elements, Elastoplastic response, Multitask learning

1 Introduction

Polycrystalline metals exhibit a strong microstructure-sensitive elastoplastic response where grain morphology, crystallographic texture, and phase topology jointly shape the onset of yielding, the evolution of hardening, and the directional character of the apparent stiffness. This sensitivity is central to multiscale modeling workflows where macroscopic predictions must reflect not only mean constitutive behavior but also variability, tails of distributions, and spatially localized hot spots that drive early-stage damage. In practice, these requirements lead to ensemble computations over many statistically distinct microstructures, and the cost of repeated high-fidelity simulations becomes the dominant bottleneck.

Computational homogenization formalizes this scale-bridging task through the use of *Representative Volume Element* (RVE), which provides an effective representation of the material's behavior once scale separation is achieved [1–4]. However, in many applications, the relevant domain is not sufficiently large to reach an RVE limit, the RVE size can be prohibitively large (particularly for nonlinear properties), or the RVE may not exist in a strict sense for certain responses such as softening

and post-peak behavior [5–9]. These limitations motivate *Statistical Volume Elements* (SVEs), which provide a continuum description via *apparent* properties that retain finite-size variability and directional dependence [10–14]. From an engineering standpoint, SVEs offer a controllable compromise: one can trade computational cost against the degree of heterogeneity preserved, while still maintaining a consistent mapping from microstructure to homogenized quantities across the sizes at which variability remains non-negligible [15–17]. Most importantly, by resulting in an inhomogeneous and random coarse-grained representation of the material microstructure, they can systematically relate material aleatory uncertainties to the distribution of macroscopic Quantities of Interest (QoIs). This propagation of statistics across scales cannot be achieved by using RVEs.

A common route to SVE-based mesoscale modeling is the moving-window method, where local apparent properties are obtained by partitioning a larger microstructural domain into a hierarchy of windows [18–22]. This construction naturally supports random-field descriptions of constitutive parameters, which are essential when spatial variability governs macroscopic failure patterns. For example, the ability to resolve intermediate-scale variability (below the RVE limit but above the grain scale) can strongly influence predicted crack paths and failure statistics [9, 15, 23]. For polycrystalline metals, the same logic applies to constitutive variability relevant to crack nucleation, where local yielding and hardening fluctuations can matter even when global averages appear well converged.

Despite their modeling value, SVEs impose a substantial computational burden when evaluated using full-field crystal plasticity. Crystal Plasticity Finite Element Method (CPFEM) simulations remain a standard tool for resolving grain-scale anisotropy and heterogeneous slip, but they are expensive in multi-phase settings and in regimes where large ensembles are required [24, 25]. Moreover, the SVE size needed for plastic descriptors can be substantially larger than that needed for elastic

descriptors, implying that the most informative statistics are often the most costly to obtain [17]. This creates a practical gap for multiscale studies that require (i) many SVEs per microstructure for block-wise random-field construction, (ii) many microstructures per material state for uncertainty quantification, and (iii) nonlinear response.

Surrogate modeling has therefore become an active strategy to accelerate microstructure-property linkages. Classical reduced-order and data-driven homogenization frameworks have demonstrated that nonlinear effective response can be learned from micromechanical simulations when suitable microstructural descriptors are available [26, 27]. Machine learning has also been used to boost nonlinear homogenization by coupling data-driven components with established homogenization formalisms [28]. More recently, deep learning has been used to approximate crystal plasticity response and related field mappings, including approaches that target CPFEM-based predictions or embed learned constitutive components into finite element workflows [29–32]. Neural operator formulations further extend this line of work by learning mappings between function spaces for stress or field prediction, with recent efforts introducing physics-aware constraints, such as preserving equilibrium [33]. While these developments are promising, microstructure representation remains a recurring challenge: image/voxel-based encodings can be data-intensive and resolution-tied, and they struggle to accommodate variable numbers of grains across SVE sizes without careful architectural choices.

Graph representations provide a principled alternative because they match the discrete topology of polycrystals. In geometric deep learning, graphs provide a native representation for irregular domains and their relational structure [34–36]. For polycrystalline microstructures, grains can be treated as nodes and grain-boundary neighborhoods as edges, enabling the encoding of crystallographic state at the node

level and misorientation-driven interactions at the edge level. Graph-based GNN surrogates have also demonstrated accurate homogenization in composite microstructures using unstructured topology-derived graphs, including prediction of tensorial stiffness and strength measures across diverse configurations [37]. This representation supports size variability (different grain counts per SVE), preserves physical interpretability, and allows message passing to model short-range mechanisms that dominate heterogeneous response. Recent mechanics-focused studies have further demonstrated the utility of GNNs for material structure-property prediction across diverse settings, including microstructure-informed elasticity and polycrystal-related tasks [38–41]. Graph-based learning has also been explored in fatigue response predictions, where localized values are of primary interest, thereby reinforcing the suitability of grain graphs for capturing rare yet consequential response modes [42]. In addition, open software ecosystems for graph learning and scientific GNN training reduce barriers to scalable surrogate deployment [43–45].

In this work, we develop a deterministic multitask graph neural network surrogate for predicting SVE-level elastoplastic responses in dual-phase polycrystals. Each SVE is represented as a grain-adjacency graph with node features encoding phase, geometry, and crystallographic orientation, and with edge features encoding relative misorientation. The surrogate learns a shared microstructure embedding via Principal Neighbourhood Aggregation (PNA) [46] message passing and predicts both scalar QoIs, including stiffness components, isotropic moduli, yield strengths, and hardening descriptors, as well as vector-valued stress–strain responses in orthogonal loading directions. Beyond pointwise accuracy, we evaluate whether the surrogate preserves finite-SVE variability across sizes and compositions in a manner consistent with SVE-based mesoscale modeling.

The main contributions of this study are:

- A grain-graph representation and multitask GNN surrogate for mapping polycrystal SVEs to elastic and plastic homogenized quantities across multiple SVE sizes.
- Joint prediction of scalar properties and full stress–strain trajectories within a shared embedding framework, supporting nonlinear response characterization beyond scalars.
- Validation at the population level (distributions and variability) to assess suitability for SVE-based block-wise random-field construction and ensemble-driven multiscale analyses.

2 Dataset Description

The dataset employed in this study is derived from the high-fidelity CPFEM simulations reported in our prior work [17]. In that work, the size dependency of homogenized elastic and plastic properties of dual-phase polycrystalline materials was systematically investigated using the SVE framework. The present study uses that validated computational database to construct a structured microstructure-property dataset suitable for deterministic surrogate modeling.

2.1 Material System and Microstructure Generation

The material system consists of dual-phase ferrite-martensite polycrystals. Three microstructural configurations were generated corresponding to martensite volume fractions (v_f) of 10% (M1), 45% (M2), and 90% (M3). Each macroscopic microstructural domain has dimensions $400\,\mu\text{m} \times 400\,\mu\text{m} \times 1\,\mu\text{m}$ with an average grain equivalent diameter of $\bar{d} = 5\,\mu\text{m}$. Grains are assumed equiaxed and assigned random crystallographic orientations sampled from a uniform orientation distribution function. Phase-dependent elastic constants and crystal plasticity parameters were assigned at the grain level. Microstructures were generated using DREAM.3D [47] and discretized for full-field CPFEM simulations.

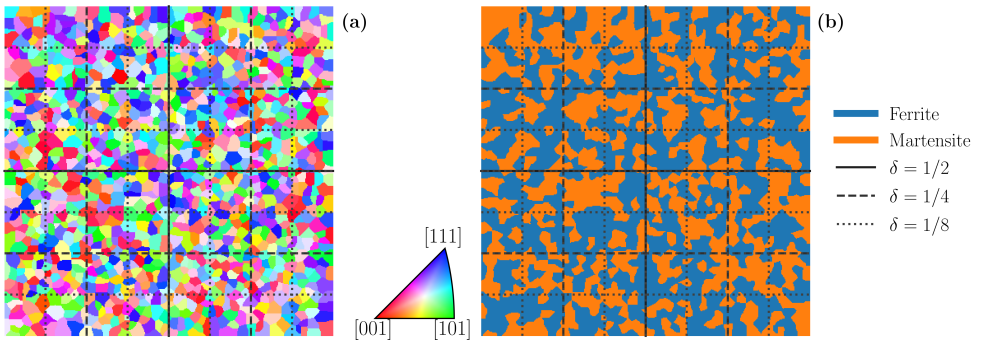

Fig. 1 Example $400\,\mu$m $\times$ $400\,\mu$m parent microstructure showing (a) grain orientations colored according to the inverse pole figure (IPF) key and (b) phase distribution for ferrite and martensite. Grid lines indicate the SVE partitioning levels corresponding to $\delta = 1/2$, $1/4$, and $1/8$.

2.2 SVE Extraction

To capture spatial variability and size effects, the SVEs were extracted using a space-filling moving-window partitioning approach. Figure 1 illustrates an example microstructure from $v_f = 0.45$, where the grain orientations are colored using inverse pole figure (IPF) and the partitions used for SVEs are plotted over the domain. The considered SVE sizes are $L_{\mathrm{SVE}} \in \{50, 100, 200, 400\}\,\mu$m, which tile 30 different 400 μm $\times$ 400 μm parent domains into 8×8, 4×4, 2×2, and 1×1 grids, respectively, without overlap or gaps. These correspond to size $\delta = L_{\mathrm{SVE}}/400\ \mu\mathrm{m} \in \{1/8, 1/4, 1/2, 1\}$. The parameter δ denotes the subdivision ratio relative to the full domain, so decreasing L_{SVE} (larger subdivision) increases the number of SVEs obtained from each parent microstructure and, consequently, the share of samples at that size. In total, there are 30, 120, 480, and 1920 samples per v_f for $\delta = 1$, $1/2$, $1/4$, and $1/8$, respectively. All SVEs are non-overlapping and collectively cover the entire domain.

This construction ensures that the dataset explicitly captures composition dependence through the martensite v_f, size dependence through the SVE length scale, and intrinsic statistical variability across different microstructural realizations. As a result,

the database systematically encodes the coupled effects of phase contrast, observation window size, and microstructural randomness on the homogenized mechanical response.

2.3 CPFEM Simulation and Homogenization

Each SVE was analyzed using a full-field crystal plasticity formulation under mixed boundary conditions (MBC). Three independent loading cases were applied, namely uniaxial tension in the x direction, uniaxial tension in the y direction, and in-plane shear loading. The homogenized stress–strain response was obtained by volume averaging the microscopic stress and strain fields. In-plane stresses and strains were expressed in Voigt notation as

$$\boldsymbol{\sigma} = \begin{bmatrix} \sigma_{xx} \\ \sigma_{yy} \\ \sigma_{xy} \end{bmatrix}, \qquad \boldsymbol{\gamma} = \begin{bmatrix} \varepsilon_{xx} \\ \varepsilon_{yy} \\ 2\varepsilon_{xy} \end{bmatrix}, \tag{1}$$

and the homogenized elastic constitutive relation was written as

$$\boldsymbol{\sigma} = \mathcal{C}\,\boldsymbol{\gamma}, \tag{2}$$

where the in-plane stiffness tensor is given by

$$\mathcal{C} = \begin{bmatrix} \mathcal{C}_{11} & \mathcal{C}_{12} & \mathcal{C}_{13} \\ \mathcal{C}_{12} & \mathcal{C}_{22} & \mathcal{C}_{23} \\ \mathcal{C}_{13} & \mathcal{C}_{23} & \mathcal{C}_{33} \end{bmatrix}. \tag{3}$$

Here, $\mathcal{C}_{33}$ denotes the in-plane shear stiffness.

2.4 Output Quantities of Interest

For each SVE, both elastic and plastic homogenized quantities were reported.

2.4.1 Elastic Properties

The elastic outputs include the in-plane stiffness components $\mathcal{C}_{11}, \mathcal{C}_{12}, \mathcal{C}_{22}, \mathcal{C}_{33}$, and bulk modulus κ together with isotropic shear modulus μ obtained through Reuss angular averaging of $\mathcal{C}$, *cf.* [5]. Although the full in-plane stiffness tensor in Eq. 3 is computed from the three CPFEM loading cases for every SVE, the present dataset is dominated by the orthotropic components $\{\mathcal{C}_{11}, \mathcal{C}_{12}, \mathcal{C}_{22}, \mathcal{C}_{33}\}$. Because the coupling terms $\mathcal{C}_{13}$ and $\mathcal{C}_{23}$ remain consistently close to zero across the dataset, only these orthotropic-dominant components are retained for learning and reporting.

2.4.2 Plastic Properties

Plastic quantities were extracted from the homogenized stress–strain curves. The yield strength Y was determined using the 0.2% offset criterion, while directional yield strengths Y_x and Y_y were computed for loading along the principal directions. The tail hardening modulus was defined as

$$H = \frac{1}{2}\left(\frac{d\sigma_{xx}}{d\varepsilon_{xx}} + \frac{d\sigma_{yy}}{d\varepsilon_{yy}}\right), \tag{4}$$

and evaluated as the average slope over the final six increments of the macroscopic stress–strain response. In addition, homogenized stress–strain curves $\sigma_{xx}(\varepsilon)$ and $\sigma_{yy}(\varepsilon)$ were sampled at 24 strain increments to characterize the nonlinear mechanical response.

2.5 Statistical Characteristics

The dataset exhibits several key characteristics. Property variance decreases with increasing SVE size, indicating the convergence toward the representative-volume-element behavior. An example convergence is given in Figure 2. Elastic and plastic

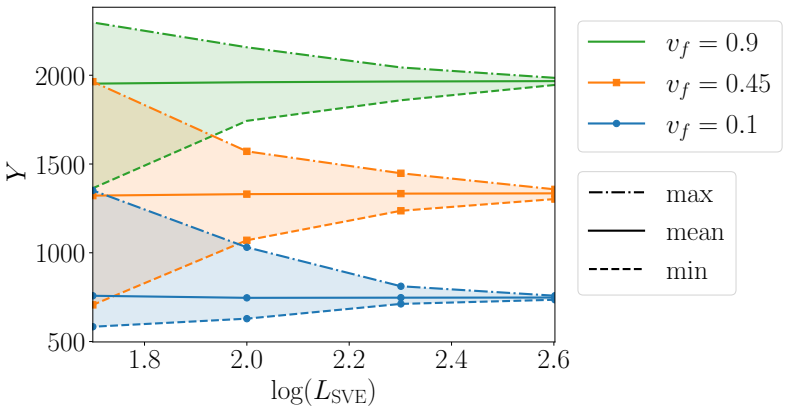

Fig. 2 Variation of the average yield strength Y (MPa) with SVE size for three martensite volume fractions plotted against $\log(L_{\mathrm{SVE}})$. Solid lines denote the mean response across SVE realizations, while dashed and dash–dotted lines represent the minimum and maximum values, respectively.

properties exhibit distinct scaling trends, with plastic quantities, particularly the hardening modulus H, showing larger variability and slower convergence. Intermediate martensite fractions exhibit increased anisotropy and statistical dispersion. Furthermore, property distributions at small SVE sizes exhibit the highest level of anisotropy and inhomogeneity. Overall, the dataset spans multiple compositions, length scales, and mechanical regimes, providing a comprehensive microstructure–property database suitable for surrogate modeling of SVE-level homogenized response.

3 Graph Neural Network Framework

Figure 3 summarizes the grain-graph surrogate used to predict SVE-level elastoplastic QoIs from dual-phase polycrystal microstructures. The framework maps each SVE to a graph, performs message passing to obtain node embeddings that encode local neighborhood interactions, and then aggregates these embeddings into a compact SVE representation that drives a multitask regression head.

Each SVE is represented as a graph $G = (\mathcal{V}, \mathcal{E})$, where $\mathcal{V}$ is the set of microstructural entities (nodes) and $\mathcal{E}$ is the set of neighborhood relations (edges). We use

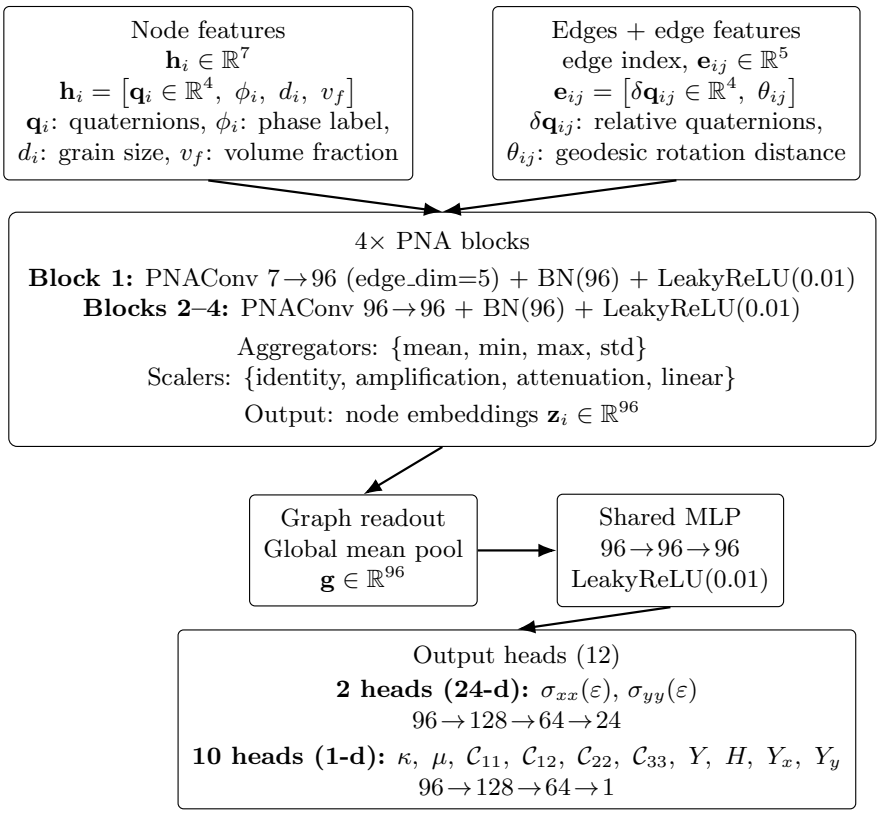

Fig. 3 Simplified PNA-based GNN: node features $\mathbf{h}_i = [\mathbf{q}_i, \phi_i, d_i, v_f]$, edge features $\mathbf{e}_{ij} = [\delta\mathbf{q}_{ij}, \theta_{ij}]$, 4 PNA blocks using the shown aggregators/scalers, global mean pooling, shared Multilayer Perceptron (MLP), and 12 prediction heads.

a grain-based VE representation because it significantly reduces input dimensionality while preserving microstructure. In grain-based graphs, each node corresponds to a grain. This choice provides a physically interpretable representation in which nodes align with crystallographic state variables (orientation, phase) and geometric descriptors (grain size).

Edges encode short-range microstructural interactions. In the grain-graph setting, we connect nodes using adjacency across grain boundaries: two grains i and j are neighbors if they share an interface in the tessellation/segmentation. We treat the graph as undirected in the physical sense, but implement it with two directed edges $(i \to j)$ and $(j \to i)$ for message passing. This construction produces sparse graphs with

locality aligned to the mechanisms that drive effective response: Phase connectivity, crystallographic misorientation, and neighboring grains.

Each node $i \in \mathcal{V}$ is assigned a feature vector $\mathbf{h}_i \in \mathbb{R}^7$ (Fig. 3)

$$\mathbf{h}_i = \left[\mathbf{q}_i \in \mathbb{R}^4,\ \phi_i,\ d_i,\ v_f\right], \tag{5}$$

where $\mathbf{q}_i$ is the grain orientation encoded as a unit quaternion[1], ϕ_i is a phase label (binary encoding for ferrite/martensite), d_i is a grain size descriptor (e.g., number of elements), and v_f is the SVE-level volume fraction. The scalar v_f is replicated to each node to provide global compositional context during message passing.

Each directed edge $(i, j) \in \mathcal{E}$ carries an edge feature vector $\mathbf{e}_{ij} \in \mathbb{R}^5$

$$\mathbf{e}_{ij} = \left[\delta\mathbf{q}_{ij} \in \mathbb{R}^4,\ \theta_{ij}\right], \tag{6}$$

where $\delta\mathbf{q}_{ij}$ is the relative quaternion between grains i and j, and θ_{ij} is the geodesic rotation distance, providing a scalar misorientation measure. This feature design separates node-level descriptors (state and geometry) from edge-level descriptors (pairwise crystallographic relationships), which is particularly relevant for plasticity-sensitive QoIs.

The surrogate is a graph neural network with four message-passing (PNA) layers. In each layer, every node (grain) updates its internal feature vector by combining its own information with information coming from its neighboring grains through the grain-boundary edges. We start from 7 input features per node and 5 features per edge; the first PNA layer maps the node description from $\mathbb{R}^7$ to a 96-component hidden representation, and the next three layers keep the same 96-dimensional size while

[1] Grain orientations are represented with unit quaternions rather than Euler angles because quaternions provide a smooth, singularity-free description of 3D rotations. In contrast, Euler angles can suffer from gimbal-lock-type singularities and discontinuities, and their representation is more redundant under crystal symmetry. For learning on grain graphs, quaternions therefore provide a more stable basis for encoding orientations and computing relative misorientations between neighboring grains.

progressively refining it as shown in Figure 3. The output of these four layers is a learned 96-dimensional vector $\mathbf{z}_i \in \mathbb{R}^{96}$ for each node, which is called a node embedding, providing a compact numerical summary of the local microstructural context around grain i.

PNA is designed to perform well when different nodes have very different numbers of neighbors. To achieve this, it summarizes each node's neighborhood in several complementary ways using the aggregators $\{\text{mean}, \text{min}, \text{max}, \text{std}\}$, and then adjusts these summaries with degree-dependent scalers $\{\text{identity}, \text{amplification}, \text{attenuation}, \text{linear}\}$. Using multiple summaries, together with degree-aware rescaling, makes the layer more stable and robust across SVEs whose grain-adjacency graphs can vary in connectivity.

Node embeddings are reduced to an SVE representation via global mean pooling

$$\mathbf{g} = \frac{1}{|\mathcal{V}|} \sum_{i \in \mathcal{V}} \mathbf{z}_i, \qquad \mathbf{g} \in \mathbb{R}^{96}. \tag{7}$$

Mean pooling provides a stable summary when the number of grains varies across SVEs and partition scales, a significant advantage over CNNs. A shared Multilayer Perceptron (MLP) refines the global mean pooling by adding three more layers and using LeakyReLU (0.01) as the activation function. The shared latent is then mapped to 12 task-specific output heads:

- Two 24-dimensional heads for stress–strain responses, $\sigma_{xx}(\varepsilon)$ and $\sigma_{yy}(\varepsilon)$, each parameterized by $96 \to 128 \to 64 \to 24$.
- Ten scalar heads for $\{\kappa, \mu, C_{11}, C_{12}, C_{22}, C_{33}, Y, H, Y_x, Y_y\}$, each parameterized by $96 \to 128 \to 64 \to 1$.

This structure enforces a shared microstructure embedding while allowing the final mappings to specialize by the QoI type (scalar versus curve).

Training minimizes a multi-output mean squared error (MSE) aggregated over all heads. Let the set of tasks be $\mathcal{T} = \{1, \ldots, 12\}$, and let task t have output dimension

d_t (with $d_t = 1$ for scalar QoIs and $d_t = 24$ for stress–strain heads). For a graph G, predictions are $\hat{\mathbf{y}}^{(t)}(G)$ and targets are $\mathbf{y}^{(t)}(G)$. The combined loss function is

$$\mathcal{L} = \frac{1}{|\mathcal{T}|} \sum_{t \in \mathcal{T}} \frac{1}{d_t} \left\| \mathbf{y}^{(t)}(G) - \hat{\mathbf{y}}^{(t)}(G) \right\|_2^2 . \tag{8}$$

The per-task normalization by d_t prevents the 24-dimensional curve heads from dominating the optimization purely by dimensionality. In practice, targets are standardized using statistics computed on the training set to reduce scale imbalance across elastic constants and plastic metrics; predictions are then mapped back to physical units for reporting.

To prevent information leakage arising from correlated SVEs extracted from the same parent microstructure, we perform an image-level split. Parent microstructure images are first divided into train/validation/test sets. Then, all SVEs derived from a given parent image are assigned to the same subset, including the full hierarchy of partitions (e.g., the $\delta = 1/1$ SVE and its corresponding $\delta = 1/2$, $\delta = 1/4$, and $\delta = 1/8$ sub-SVEs). We target equal representation for each martensite v_f regime within each subset (stratified by v_f), and we preserve representation across SVE sizes through hierarchical assignment. In the representative split used for the main experiments, selection is performed at the image level (e.g., 26 parent images for training and 4 parent images for testing), after which all corresponding partition-derived SVEs are included automatically in the same subset.

Table 1 summarizes the SVE sampling strategy and the resulting dataset composition. For each martensite $v_f \in \{0.10, 0.45, 0.90\}$, we consider 30 parent microstructures over a 400 μm $\times$ 400 μm domain and extract non-overlapping SVEs of L_{SVE} and δ as explained in Section 2. The table also reports the average grain count per SVE, emphasizing that smaller observation windows contain fewer grains and therefore represent more localized microstructural environments. As a representative measure

Table 1 Summary of the SVE dataset (derived from Anto *et al.* [17] for three martensite volume fractions: $v_f = \{0.10, 0.45, 0.90\}$, with 30 parent microstructures per v_f). Coefficient of variance (CoV) of Y is given as an example.

L_{SVE} [μm]	δ	Avg. grain count	Samples per v_f	Share [%]	CoV(Y)
400	1/1	1180	30	1.2	0.006
200	1/2	315	120	4.7	0.023
100	1/4	89	480	18.8	0.051
50	1/8	27	1920	75.3	0.113

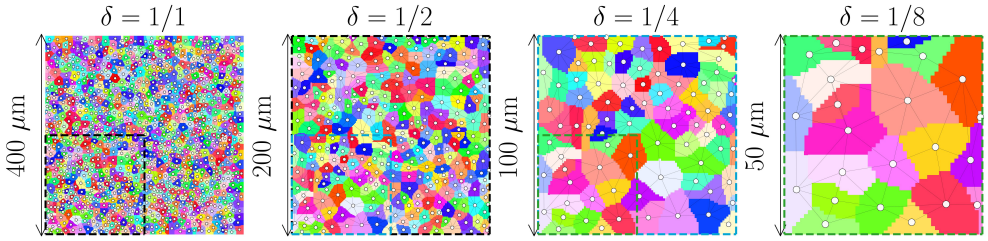

Fig. 4 Example microstructure domains at four SVE sizes together with the corresponding grain-graph representations used as inputs to the GNN model.

of size-dependent scatter, the coefficient of variation (CoV) of the yield strength Y is listed; the monotonic increase in CoV with decreasing L_{SVE} reflects stronger microstructural variability at smaller length scales. Figure 4 illustrates an example domain and corresponding graph from each size referenced in Table 1.

4 Results

This section evaluates the predictive performance and physical consistency of the proposed multitask grain-graph surrogate. We first examine whether a single model trained on multiple martensite volume fractions can maintain accuracy across individual composition regimes (Section 4.1). This analysis establishes that pooling data across volume fractions enables a unified surrogate while preserving most predictive fidelity. We then quantify the accuracy of scalar elastic and plastic quantities of interest using parity plots, highlighting regions where the model achieves strong agreement

Table 2 Effect of pooling volume fractions during training. $R^2_{\text{spec}}(v_f)$ denotes within-regime R^2 for a model trained only on regime v_f and evaluated on test SVEs from the same regime. $R^2_{\text{unif}|v_f}$ denotes within-regime R^2 for the unified model $\mathcal{M}_{\text{all}}$ evaluated on the test subset restricted to regime v_f. The pooled scores compare (i) concatenated predictions from specialized models (each test sample predicted by its regime-specific model; columns 2 to 7) and (ii) a single unified model evaluated on the concatenated test set (columns 8 and 9).

QoI	R^2_{spec}			$R^2_{\text{unif}\|v_f}$			$\cup v_f$	
	v_f=0.1	v_f=0.45	v_f=0.9	v_f=0.1	v_f=0.45	v_f=0.9	${R^2_{\text{spec}}}^{\text{pool}}$	${R^2_{\text{unif}}}^{\text{pool}}$
$\mathcal{C}_{11}$	0.881	0.905	0.761	0.865	0.863	0.751	0.993	0.990
$\mathcal{C}_{12}$	0.734	0.762	0.392	0.704	0.714	0.422	0.969	0.969
$\mathcal{C}_{22}$	0.894	0.910	0.768	0.869	0.880	0.738	0.993	0.991
$\mathcal{C}_{33}$	0.143	0.209	0.075	0.152	0.209	0.103	0.807	0.828
κ	0.966	0.962	0.919	0.931	0.940	0.908	0.998	0.996
μ	0.504	0.564	0.247	0.550	0.565	0.335	0.947	0.950
Y	0.792	0.853	0.586	0.771	0.812	0.611	0.987	0.985
H	0.594	0.745	0.323	0.571	0.648	0.403	0.964	0.966
Y_x	0.779	0.843	0.577	0.738	0.799	0.605	0.986	0.985
Y_y	0.734	0.848	0.561	0.748	0.812	0.591	0.986	0.984

with CPFEM results (Section 4.2). Next, we evaluate vector-valued stress–strain predictions in the x and y loading directions using both curve-level metrics and population envelopes to assess fidelity in nonlinear response and variability (Section 4.3). Finally, we examine whether the surrogate preserves microstructural heterogeneity across SVE partitions by comparing predicted and reference distributions and spatial field patterns (Sections 4.4).

4.1 Volume-fraction generalization

To assess whether a single model can generalize across martensite volume fractions without sacrificing accuracy, we compare two training strategies: (i) v_f*-specific* models trained on a single regime, and (ii) a *unified* model trained on the pooled dataset spanning all v_f. Let $\mathcal{D}_{v_f}$ denote the subset of SVEs with volume fraction $v_f \in \{0.10, 0.45, 0.90\}$. We train specialized models $\mathcal{M}_{v_f}$ on $\mathcal{D}_{v_f}$ and a unified model $\mathcal{M}_{\text{all}}$ on $\bigcup_{v_f} \mathcal{D}_{v_f}$. For evaluation, we report two complementary coefficients of determination: (a) *within-regime* (conditional) scores, $R^2(\mathcal{M}, \mathcal{D}^{\text{test}}_{v_f})$, computed on test SVEs restricted to a fixed v_f, and (b) *pooled* scores computed after concatenating all test

SVEs across regimes. For the pooled score using specialized models, each test sample is predicted by its corresponding $\mathcal{M}_{v_f}$ (a post-hoc regime-aware reference), whereas the unified pooled score uses $\mathcal{M}_{\text{all}}$ for all samples.

Before comparing regime-specific and unified training strategies, it is useful to note that direct cross-volume-fraction transfer is generally poor when a model is trained on a single composition regime and evaluated on another. As an illustrative example, Appendix Figure A1 shows parity plots for a model trained only on $vf = 0.10$ and tested on $v_f = 0.45$, where several scalar QoIs exhibit substantial degradation. This behavior motivates the volume-fraction generalization study below and supports the use of a unified model trained on pooled v_f data.

Table 2 shows that unified training does not degrade performance in a systematic way: the conditional R^2 values of $\mathcal{M}_{\text{all}}$ remain close to those of the specialized $\mathcal{M}_{v_f}$ models across most outputs, while eliminating the need to maintain separate models for each composition regime. Moreover, the pooled R^2 from the unified model is comparable to that obtained by combining specialized models, indicating that a single set of learned microstructure features can support accurate predictions across volume fractions. The main exception is the direction-dependent shear component C_{33}, which remains challenging for both strategies; however, even for this case, the unified pooled score is competitive, consistent with the broader observation that shear-dominated response is particularly sensitive to finite-SVE anisotropy effects, which is explained in detail in the next section.

Table 2 should therefore be interpreted in two complementary ways. The unified model remains competitive with the regime-specific models within individual v_f regimes, but the strongest gains are observed in the pooled evaluation, where the model benefits from learning the broader variation in responses across compositions. Accordingly, the main result is not that pooled training is uniformly superior across all regimes, but that a single unified surrogate preserves most within-regime fidelity

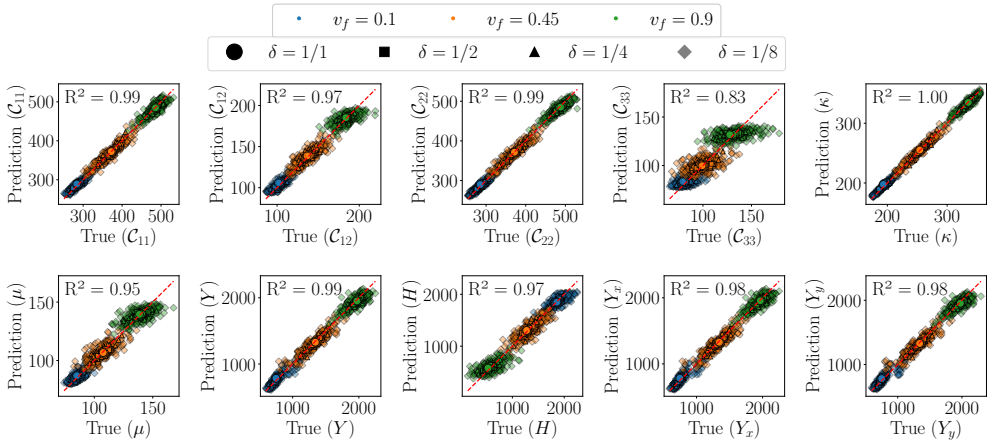

Fig. 5 Parity plots for the linear and nonlinear scalar QoIs.

while also capturing the dominant cross-regime trends. Here, the pooled R^2 primarily measures fidelity across the broader response range obtained by combining all v_f regimes, whereas the conditional R^2 is the stricter measure of within-regime sensitivity at fixed v_f.

4.2 Elastic and plastic QoIs

Figure 5 reports parity plots for the ten scalar QoIs. All stiffness and strength units in the manuscript are MPa. Overall, the surrogate achieves very high accuracy for both elastic and plastic properties, indicating that the learned SVE embedding is sufficiently expressive to resolve microstructure-induced trends beyond simple compositional averaging. The best-performing elastic targets are C_{11} and C_{22}, followed by C_{12}. The derived isotropic bulk modulus κ exhibits the highest agreement among the reported scalars with an R^2 higher than 0.995, while the isotropic shear modulus μ remains strongly correlated ($R^2 = 0.95$). These results suggest that the model captures both the principal stiffness response and derived moduli consistently within a single multitask representation.

Plastic scalars show a similarly strong performance. The yield strength Y is predicted with $R^2 = 0.99$ and the hardening descriptor H with $R^2 = 0.97$. Directional yield strengths are predicted with nearly identical accuracy in both loading directions (Y_x: $R^2 = 0.98$, Y_y: $R^2 = 0.98$); this is particularly important for maintaining directional consistency when SVEs exhibit apparent anisotropy due to finite sampling and phase topology. The parity scatter plots for these plastic quantities remain concentrated near the identity line, indicating that the surrogate preserves relative ranking across SVEs and does not systematically bias toward the mean.

Among the elastic scalars, shear modulus C_{33} exhibits the largest dispersion ($R^2 = 0.83$), despite the high accuracy obtained for isotropic shear modulus μ ($R^2 = 0.95$). This contrast suggests that the dominant challenge is not capturing the overall elastic stiffness level, but resolving the direction-dependent shear response that emerges at finite SVE sizes. In particular, C_{33} is more strongly influenced by the microstructure topology, including phase connectivity, interface networks, and local constraint pathways, than the angle-averaged response encoded in μ. At small-to-intermediate SVE sizes, these topology-driven effects can also manifest as apparent anisotropy, even when the parent microstructure is statistically isotropic, thereby increasing sample-to-sample variability and reducing the predictability of a single shear component. The relatively higher dispersion of C_{33} is also influenced by the MBC used in the crystal plasticity simulations. In the adopted formulation, roller-type constraints are applied on certain faces of the SVE. These constraints work well for the normal loading cases that provide C_{11} and C_{22}. However, C_{33} is obtained from the shear loading case, which appears to be more sensitive to this boundary treatment. As a result, the shear response obtained from the SVE simulations may contain additional variability compared with the normal stiffness components[2]. This interpretation is also consistent

[2]Other types of MBC [48–50] may provide a more accurate shear response. The corresponding C_{33} values could correlate more strongly with the microstructure and therefore show lower dispersion in the surrogate GNN model. However, the original CP dataset used in this work did not include results obtained with such alternative boundary conditions.

with our prior CPFEM study of the same SVE database, where the shear modulus exhibited smaller convergence rates and larger RVE sizes than the bulk modulus, indicating stronger sensitivity of shear-dominated quantities to finite-SVE variability and anisotropy [17].

Finally, the evaluation is designed to measure generalization at the parent-image level. The train and test split is performed on microstructure images with stratification across v_f regimes, and all partition-derived SVEs from a given parent image are kept in the same split as explained in Section 3. The high parity agreement across scalars, therefore, reflects transfer to unseen microstructures rather than interpolation among correlated subwindows.

4.3 Stress–strain response

We next evaluate the vector-valued stress–strain targets, $\sigma_{xx}(\varepsilon)$ and $\sigma_{yy}(\varepsilon)$, each represented as a 24-dimensional output. Figure 6 summarizes population envelopes (median and 5–95% bands) across the considered volume-fraction regimes and loading directions. The surrogate reproduces the median curve shape across the full strain range, including the initial elastic regime, the yield transition, and subsequent hardening. This indicates that the shared latent embedding captures the coupled features needed to predict both elastic slope and post-yield evolution.

A key outcome is the agreement in response variability. The predicted 5–95% envelopes track the observed spread, suggesting that the surrogate preserves heterogeneity across SVEs rather than collapsing to a narrow mean response. This matters for downstream reliability and damage analyses, where variability and extremes (not only averages) govern initiation and uncertainty. Visually, the agreement is maintained across all volume-fraction regimes, supporting the model's ability to represent both stiffness/strength shifts and changes in scatter with microstructure.

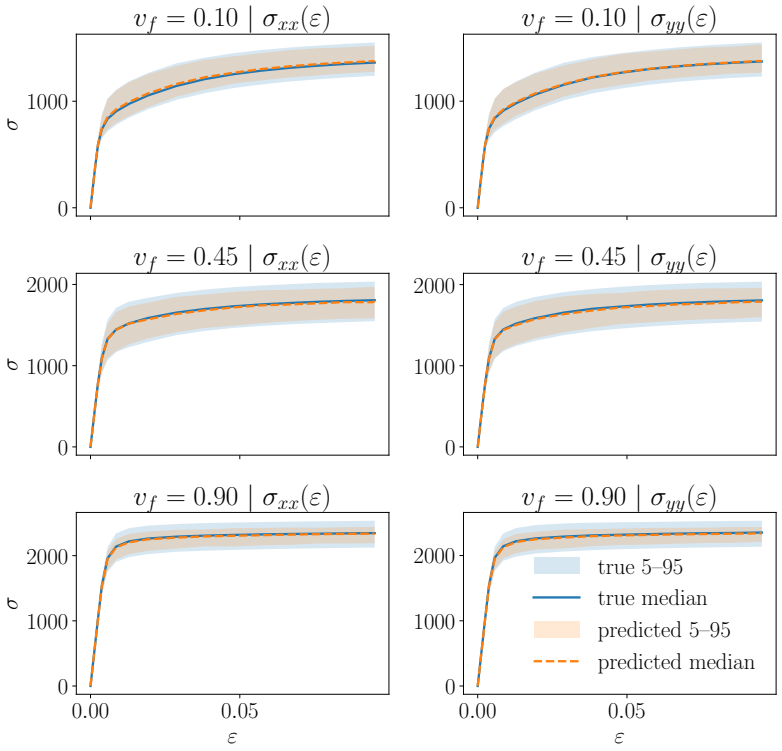

Fig. 6 Population envelopes for predicted and reference stress–strain responses under uniaxial loading in the x and y directions. For each martensite volume-fraction regime ($v_f = 0.10$, 0.45, and 0.90), the solid curves denote the reference median response and the shaded region indicates the 5–95% interval across SVE realizations.

Quantitative curve metrics are summarized in Table 3. We report R^2 to assess the explained variance of the full discretized response, and MAE/RMSE to quantify the average and quadratic errors in stress magnitude, respectively, across the sampled strain points. To enable comparison across regimes with different stress scales, we also report normalized values relative to the peak reference stress ($\mathrm{NRMSE}_{\mathrm{peak}}$). Finally, the L_∞ error captures the worst-case pointwise deviation across the strain grid, highlighting localized mismatches near the yield surface or in regions of high curvature. Across both loading directions, these metrics indicate comparable accuracy, supporting the conclusion that the surrogate does not over-specialize to a single loading axis and can represent directional stress–strain trajectories within the same multitask model.

Table 3 Curve-level performance metrics for predicted stress–strain responses in the x and y loading directions. Metrics are computed over the discretized strain grid for each response and then aggregated over the evaluation set.

Output	R^2	MAE (MPa)	RMSE (MPa)	$\mathrm{NRMSE}_{\mathrm{peak}}$ (%)	L_∞ (MPa)
$\sigma_{xx}(\varepsilon)$	0.9561	154.33	194.05	7.17	307.10
$\sigma_{yy}(\varepsilon)$	0.9558	159.94	195.28	7.29	284.60

4.4 Distributions and spatial consistency

Beyond pointwise accuracy, we evaluate whether the surrogate model preserves pointwise distribution and spatial consistency induced by SVE partitioning. Figure 7 compares predicted and reference probability density functions (PDFs) for representative scalars (κ, μ, Y, and H) across multiple partition scales. Across regimes, the predicted PDFs closely follow the reference PDFs in both the value range and the local maxima, indicating that the model reproduces not only mean shifts but also the variability structure associated with finite SVEs. This is a nontrivial requirement for microstructure surrogates, since distributional fidelity is typically more stringent than the minimization of average error.

We also assess the spatial consistency of homogenized fields using subdomain maps shown in Figure 8. The predicted fields reproduce the dominant spatial patterns across subwindows, and the corresponding error maps remain localized rather than exhibiting global bias. This behavior suggests that the model learns microstructure-dependent heterogeneity and spatial consistency that are consistent across partition levels. This is particularly relevant when partitioned predictions are later assembled into larger domains within a multiscale method, as in [51].

Taken together, the pointwise distribution and field-level comparisons indicate that the surrogate model accurately represents the underlying material heterogeneity, which is important for downstream damage and fatigue modeling. In such settings, localized response patterns and the tails of property distributions can dominate the risk of crack

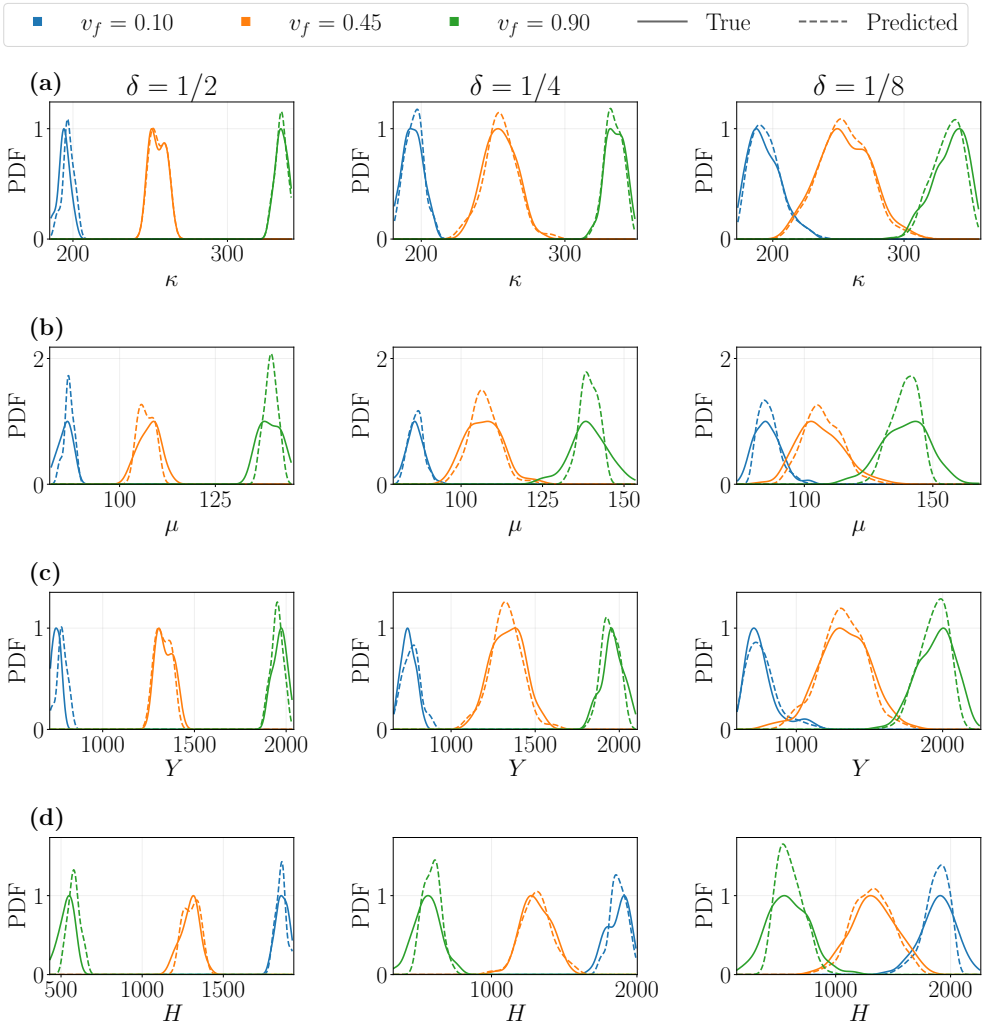

Fig. 7 Comparison of predicted and reference probability density functions (PDFs) for representative scalar QoIs across SVE partition scales and martensite volume fractions. Solid lines denote reference PDFs and dashed lines denote surrogate-predicted PDFs for (a) κ, (b) μ, (c) Y, and (d) H at partition scales $\delta \in \{1/2, 1/4, 1/8\}$.

nucleation, even when global averages appear well predicted. Moreover, retaining distributional fidelity enables the construction of statistically consistent random fields for mesoscale simulations, in which one seeks to populate larger structural domains with spatially varying elastic and fracture constitutive parameters while matching the target

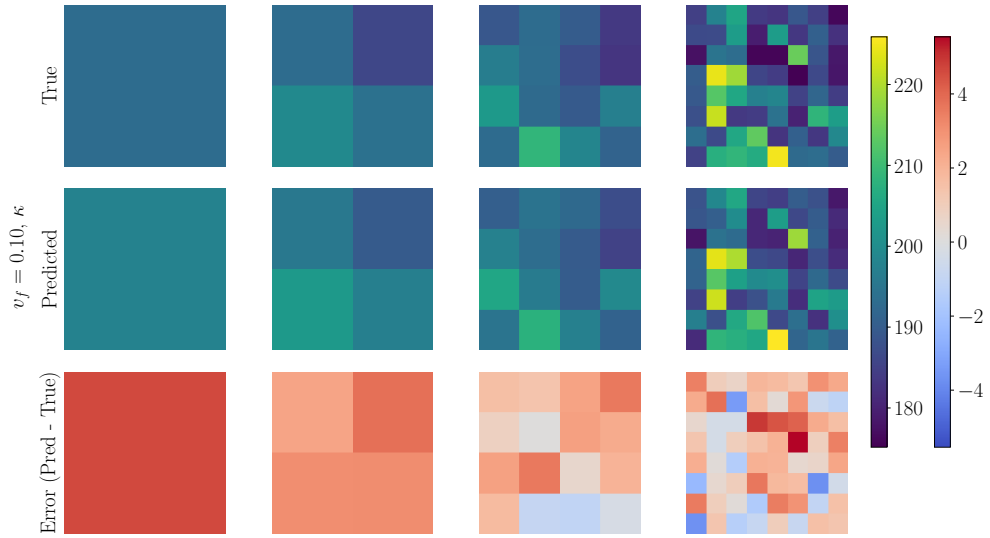

Fig. 8 Spatial consistency of surrogate predictions across SVE partitions. For a representative case, subdomain maps are shown for the reference field, the surrogate-predicted field, and the corresponding error field for the selected QoI (κ) at progressively finer partition resolutions.

n-point statistics. Such random-field representations are particularly useful for uncertainty propagation, reliability analysis, and large-area fracture/fatigue assessments, where explicitly resolving microstructure everywhere is infeasible with direct numerical simulations (DNS), yet preserving the correct variability and spatial heterogeneity remains essential and feasible, with the proposed SVE-based upscaling approach.

5 Conclusions

This work developed and evaluated a multitask grain-graph surrogate for predicting SVE-level elastoplastic response from dual-phase polycrystal microstructures. The main conclusions are as follows:

1. **Accurate multitask prediction of coupled elastic and plastic scalars.** Parity analyses demonstrate strong performance across most scalar QoIs, including stiffness components, isotropic moduli, and plastic descriptors (yield strength and

hardening). The consistent accuracy across both elastic and plastic targets indicates that a shared microstructure embedding can capture coupled trends without training independent models for each QoI.

2. **High-fidelity stress–strain trajectory prediction with directional consistency.** The surrogate predicts discretized stress–strain responses in both x and y loading directions with strong agreement in median behavior and variability envelopes. Curve-level metrics (Table 3) indicate that the overall error and explained variance are comparable across directions, supporting stable directional generalization within a single multitask architecture.
3. **Distributional and spatial agreement under SVE partitioning.** Predicted PDFs closely match the reference PDFs across partition scales and volume-fraction regimes. Moreover, partition-level field maps reproduce the dominant spatial patterns and exhibit localized residual errors. These results show that the model preserves microstructure-driven heterogeneity rather than collapsing to a mean response, which is essential when downstream analyses depend on pointwise distribution and spatial consistency.
4. **Implications for damage and fatigue modeling at larger scales.** The surrogate provides rapid microstructure-conditioned constitutive predictions that can support high-throughput screening, uncertainty propagation, and statistical characterization of mesoscale property fields. In particular, the demonstrated distributional fidelity enables construction of statistically consistent random fields for larger-domain simulations, where spatially varying constitutive parameters or strength proxies are required but explicit microstructure resolution everywhere is impractical. The ability to preserve tail behavior and spatial heterogeneity is particularly relevant to crack nucleation and early damage processes driven by localized extremes.

Overall, the proposed grain-graph surrogate demonstrates that physics-informed microstructure descriptors combined with message passing and multitask learning can accurately reproduce both scalar homogenized properties and full nonlinear stress–strain trajectories, while maintaining the variability structure induced by finite SVEs. These capabilities align with the needs of modern fracture and fatigue modeling workflows that increasingly rely on AI-assisted coarse-graining and large-scale computational studies.

Author contribution

Erdem Caliskan: Writing – original draft, Visualization, Investigation, Validation, Methodology, Software, Data curation, Formal analysis. **Anik Das Anto:** Writing – review and editing, Data curation, Investigation, Validation, Methodology, Software. **Massimiliano Lupo Pasini:** Writing – review and editing, Conceptualization, Funding acquisition, Methodology. **Stephanie TerMaath:** Writing – review and editing, Conceptualization, Project administration, Funding acquisition, Methodology. **Reza Abedi:** Writing – review and editing, Supervision, Conceptualization, Formal analysis, Project administration, Funding acquisition, Methodology.

Code availability

The open-source HydraGNN library [44], used to generate the numerical results described in this article, can be accessed at the following GitHub repository: https://github.com/ORNL/HydraGNN/tree/cp2d_paper. The scripts used in this work are located under examples/cp2d.

Data availability

The datasets generated and analyzed during this study have been deposited in Zenodo under the reserved DOI 10.5281/zenodo.19041349. The repository will be made publicly available upon acceptance/publication of this manuscript.

Ethics declaration

Not applicable.

Declaration of Competing Interest

Erdem Caliskan reports that financial support was provided by Oak Ridge Institute for Science and Education (ORISE). The other authors declare that they have no known competing financial interests or personal relationships that could have appeared to influence the work reported in this paper.

Acknowledgements

Massimiliano Lupo Pasini and Erdem Caliskan thank Dr. Vladimir Protopopescu for his valuable feedback in the preparation of the manuscript.

This research is sponsored by the Artificial Intelligence Initiative as part of the Laboratory Directed Research and Development (LDRD) Program of Oak Ridge National Laboratory, managed by UT-Battelle, LLC, for the US Department of Energy under contract DE-AC05-00OR22725. This work used resources of the Oak Ridge Leadership Computing Facility, which is supported by the Office of Science of the U.S. Department of Energy under Contract No. DE-AC05-00OR22725, under ASCR Leadership Computing Challenge (ALCC) award LRN070.

This research was supported in part by the Air Force Office of Scientific Research (AFOSR) under grant number FA9550-22-1-0359. Erdem Caliskan acknowledges partial support by an appointment to the Oak Ridge National Laboratory GRO Program, sponsored by the U.S. Department of Energy and administered by the Oak Ridge Institute for Science and Education (ORISE).

The authors would also like to thank the University of Tennessee Infrastructure for Scientific Applications and Advanced Computing (ISAAC). A portion of the computation for this work was performed with ISAAC computational resources.

Appendix A Cross-volume-fraction transfer example

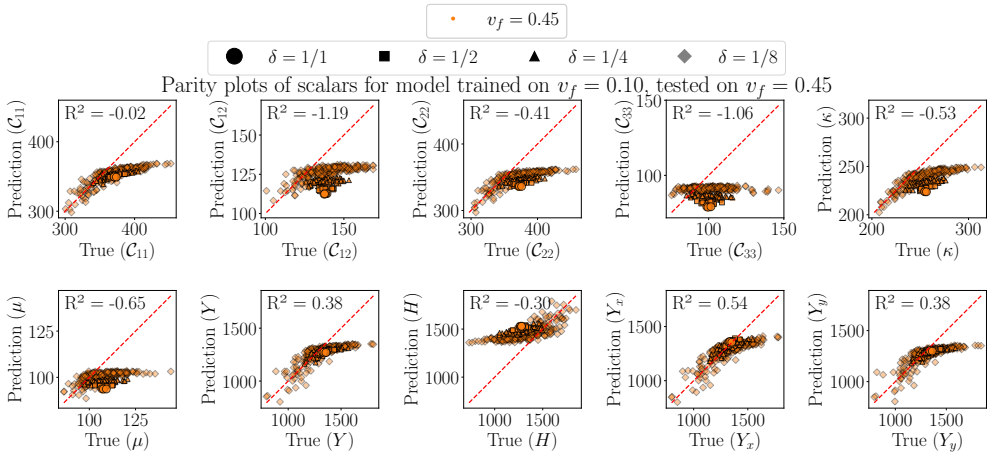

Fig. A1 Parity plots for scalar QoIs for a model trained on $v_f = 0.10$ and evaluated on $v_f = 0.45$. Marker shape denotes the SVE partition scale δ. The noticeable loss of accuracy across several outputs indicates limited direct transferability between composition regimes, motivating the pooled volume-fraction training strategy discussed in Section 4.1.

References

[1] K. Sab, On the homogenization and the simulation of random materials. Eur. J. Mech,. A/Solids **11**(5), 585–607 (1992)

[2] M. Ostoja-Starzewski, X. Du, Z. Khisaeva, W. Li, Comparisons of the size of the representative volume element in elastic, plastic, thermoelastic, and permeable random microstructures. International Journal for Multiscale Computational Engineering **5**(2) (2007)

[3] S. Nemat-Nasser, M. Hori, *Micromechanics: overall properties of heterogeneous materials*, vol. 37 (Elsevier, Amsterdam, The Netherlands, 2013)

[4] S. Stapleton, L. Appel, J.W. Simon, S. Reese, Representative volume element for parallel fiber bundles: Model and size convergence. Composites Part A: Applied Science and Manufacturing **87**, 170–185 (2016)

[5] M. Ostoja-Starzewski, Random field models of heterogeneous materials. International Journal of Solids and Structures **35**(19), 2429–2455 (1998)

[6] T. Kanit, S. Forest, I. Galliet, V. Mounoury, D. Jeulin, Determination of the size of the representative volume element for random composites: statistical and numerical approach. International Journal of solids and structures **40**(13-14), 3647–3679 (2003)

[7] I. Gitman, H. Askes, L. Sluys, Representative volume: Existence and size determination. Engineering fracture mechanics **74**(16), 2518–2534 (2007)

[8] C. Pélissou, J. Baccou, Y. Monerie, F. Perales, Determination of the size of the representative volume element for random quasi-brittle composites. International Journal of Solids and Structures **46**(14-15), 2842–2855 (2009)

[9] R. Abedi, J. Garrard, K. Acton, Elastic and strength properties of statistical volume elements: Determination of isotropic and homogeneous size limits. Computers & structures **277**, 106959 (2023)

[10] S.C. Baxter, L.L. Graham, Characterization of random composites using moving-window technique. Journal of Engineering Mechanics **126**(4), 389–397 (2000)

[11] L. Huyse, M.A. Maes, Random field modeling of elastic properties using homogenization. Journal of Engineering Mechanics **127**(1), 27–36 (2001)

[12] M. Ostoja-Starzewski, Material spatial randomness: From statistical to representative volume element. Probabilistic engineering mechanics **21**(2), 112–132 (2006)

[13] N. Tregger, D. Corr, L. Graham-Brady, S. Shah, Modeling the effect of mesoscale randomness on concrete fracture. Probabilistic Engineering Mechanics **21**(3), 217–225 (2006)

[14] M. Salmi, F. Auslender, M. Bornert, M. Fogli, Apparent and effective mechanical properties of linear matrix-inclusion random composites: Improved bounds for the effective behavior. International Journal of Solids and Structures **49**(10), 1195–1211 (2012)

[15] J.M. Garrard, R. Abedi, Statistical volume element averaging scheme for fracture of quasi-brittle materials. Computers and Geotechnics **117**, 103229 (2020)

[16] J.M. Garrard, R. Abedi, Statistical volume elements for the characterization of angle-dependent fracture strengths in anisotropic microcracked materials. ASCE-ASME Journal of Risk and Uncertainty in Engineering Systems, Part B: Mechanical Engineering **6**(2), 021008 (2020)

[17] A.D. Anto, R. Fleishel, S. TerMaath, R. Abedi, Size dependency of elastic and plastic properties of metallic polycrystals using statistical volume elements. Applied Sciences **14**(18), 8207 (2024)

[18] L. Graham, S. Baxter, Simulation of local material properties based on moving-window gmc. Probabilistic Engineering Mechanics **16**(4), 295–305 (2001)

[19] L. Graham-Brady, E. Siragy, S. Baxter, Analysis of heterogeneous composites based on moving-window techniques. Journal of engineering mechanics **129**(9), 1054–1064 (2003)

[20] K. Acton, L. Graham-Brady, *Fitting an Anisotropic Yield Surface Using the Generalized Method of Cells* (Springer Netherlands, Dordrecht, 2009), pp. 27–41

[21] K. Acton, L. Graham-Brady, Meso-scale modeling of plasticity in composites. Computer methods in applied mechanics and engineering **198**(9-12), 920–932 (2009)

[22] K. Acton, L. Graham-Brady, Elastoplastic mesoscale homogenization of composite materials. Journal of engineering mechanics **136**(5), 613–624 (2010)

[23] K.A. Acton, S.C. Baxter, B. Bahmani, P.L. Clarke, R. Abedi, Voronoi tessellation based statistical volume element characterization for use in fracture modeling. Computer Methods in Applied Mechanics and Engineering **336**, 135–155 (2018)

[24] A. Asgharzadeh, T. Park, S. Nazari Tiji, F. Pourboghrat, A computationally efficient multiscale, multi-phase modeling approach based on cpfem to assess the effect of second phase particles on mechanical properties. Crystals **13**(8), 1199 (2023)

[25] J.N. Fuhg, L. van Wees, M. Obstalecki, P. Shade, N. Bouklas, M. Kasemer, Machine-learning convex and texture-dependent macroscopic yield from crystal plasticity simulations. Materialia **23**, 101446 (2022)

[26] M.I. Latypov, S.R. Kalidindi, Data-driven reduced order models for effective yield strength and partitioning of strain in multiphase materials. Journal of Computational Physics **346**, 242–261 (2017)

[27] M.I. Latypov, L.S. Toth, S.R. Kalidindi, Materials knowledge system for nonlinear composites. Computer Methods in Applied Mechanics and Engineering **346**, 180–196 (2019)

[28] M. Tannous, C. Ghnatios, O. Castelnau, P.P. Castañeda, F. Chinesta, Machine learning-boosted nonlinear homogenization. Mechanics of Materials **201**, 105229 (2025)

[29] J.N. Heidenreich, M.B. Gorji, D. Mohr, Modeling structure-property relationships with convolutional neural networks: Yield surface prediction based on microstructure images. International Journal of Plasticity **163**, 103506 (2023)

[30] Y. He, Y. Heider, B. Markert, Embedding an ann-based crystal plasticity model into the finite element framework using an abaqus user-material subroutine. arXiv preprint arXiv:2410.08214 (2024)

[31] G.D. Pasparakis, L. Graham-Brady, M.D. Shields, Bayesian neural networks for predicting uncertainty in full-field material response. Computer Methods in Applied Mechanics and Engineering **433**, 117486 (2025)

[32] Y. Mao, S. Keshavarz, M.N.T. Kilic, K. Wang, Y. Li, A.C. Reid, W.k. Liao, A. Choudhary, A. Agrawal, A deep learning-based crystal plasticity finite element model. Scripta Materialia **254**, 116315 (2025)

[33] M.S. Khorrami, P.K. Goyal, J.R. Mianroodi, B. Svendsen, P. Benner, D. Raabe, Divergence-free neural operators for stress field modeling in polycrystalline materials. arXiv preprint arXiv:2408.15408 (2024)

[34] M.M. Bronstein, J. Bruna, Y. LeCun, A. Szlam, P. Vandergheynst, Geometric deep learning: going beyond euclidean data. IEEE Signal Processing Magazine **34**(4), 18–42 (2017)

[35] Z. Wu, S. Pan, F. Chen, G. Long, C. Zhang, P.S. Yu, A comprehensive survey on graph neural networks. IEEE transactions on neural networks and learning systems **32**(1), 4–24 (2020)

[36] B. Sanchez-Lengeling, E. Reif, A. Pearce, A.B. Wiltschko, A gentle introduction to graph neural networks. Distill **6**(9), e33 (2021)

[37] E. Caliskan, R. Abedi, M.L. Pasini, Graph neural networks for mechanical property prediction of 2d fiber composites. Materials & Design p. 114500 (2025)

[38] Y. Zhao, H. Li, H. Zhou, H.R. Attar, T. Pfaff, N. Li, A review of graph neural network applications in mechanics-related domains. Artificial Intelligence Review **57**(11), 315 (2024)

[39] M. Dai, M.F. Demirel, Y. Liang, J.M. Hu, Graph neural networks for an accurate and interpretable prediction of the properties of polycrystalline materials. npj Computational Materials **7**(1), 103 (2021)

[40] M. Dai, M.F. Demirel, X. Liu, Y. Liang, J.M. Hu, Graph neural network for predicting the effective properties of polycrystalline materials: A comprehensive analysis. Computational Materials Science **230**, 112461 (2023)

[41] Y. Qin, S. DeWitt, B. Radhakrishnan, G. Biros, Graingnn: A dynamic graph neural network for predicting 3d grain microstructure. Journal of Computational Physics **510**, 113061 (2024)

[42] G.J. Sim, M.G. Lee, M.I. Latypov, Fip-gnn: Graph neural networks for scalable prediction of grain-level fatigue indicator parameters. Scripta Materialia **255**, 116407 (2025)

[43] M. Fey, J.E. Lenssen, Fast graph representation learning with pytorch geometric. arXiv preprint arXiv:1903.02428 (2019)

[44] M. Lupo Pasini, J.Y. Choi, K. Mehta, P. Zhang, R. Weaver, A. Chowdhury, C. Li, Z. Ye, J. Baker, Hydragnn v4. 0. Tech. rep., Oak Ridge National Laboratory (ORNL), Oak Ridge, TN (United States) (2025)

[45] M.L. Pasini, G.S. Jung, S. Irle, Graph neural networks predict energetic and mechanical properties for models of solid solution metal alloy phases. Computational Materials Science **224**, 112141 (2023)

[46] G. Corso, L. Cavalleri, D. Beaini, P. Liò, P. Veličković, Principal neighbourhood aggregation for graph nets. Advances in neural information processing systems **33**, 13260–13271 (2020)

[47] M.A. Groeber, M.A. Jackson, Dream. 3d: a digital representation environment for the analysis of microstructure in 3d. Integrating materials and manufacturing innovation **3**(1), 56–72 (2014)

[48] C. Huet, Application of variational concepts to size effects in elastic heterogeneous bodies. Journal of the Mechanics and Physics of Solids **38**(6), 813–841 (1990)

[49] S. Hazanov, C. Huet, Order relationships for boundary conditions effect in heterogeneous bodies smaller than the representative volume. Journal of the Mechanics and Physics of Solids **42**(12), 1995–2011 (1994)

[50] S. Hazanov, M. Amieur, On overall properties of elastic heterogeneous bodies smaller than the representative volume. International Journal of Engineering Science **33**(9), 1289–1301 (1995)

[51] B. Bahmani, M. Yang, A. Nagarajan, P.L. Clarke, S. Soghrati, R. Abedi, Automated homogenization-based fracture analysis: Effects of sve size and boundary condition. Computer Methods in Applied Mechanics and Engineering **345**, 701–727 (2019)